Eur. J. Mineral., 35, 347–360, 2023
https://doi.org/10.5194/ejm-35-347-2023


European Journal of Mineralogy
Open Access

# Late metamorphic veins with dominant PS-15 polygonal serpentine in the Monte Avic ultramafite

**Luca Barale[1,5], Giancarlo Capitani[2], Paolo Castello[3], Roberto Compagnoni[4,5], Roberto Cossio[4,5], Gianluca Fiore[6], Linda Pastero[4], and Marcello Mellini[5]**

[1]Institute of Geosciences and Earth Resources, National Research Council (CNR) of Italy, Via Valperga Caluso 35, 10125 Turin, Italy
[2]Dept. of Earth and Environmental Sciences (DISAT), University of Milano-Bicocca, 20126 Milan, Italy
[3]Freelance Geologist and Researcher: Regione Saraillon 26, 11100 Aosta, Italy
[4]Dept. of Earth Sciences, University of Turin, Via Valperga Caluso 35, 10125 Turin, Italy
[5]"G. Scansetti" Interdepartmental Center for Studies on Asbestos and Other Toxic Particulates, University of Turin, Via Pietro Giuria 7, 10125 Turin, Italy
[6]Dept. of Chemistry and Interdepartmental Center for Nanostructured Interfaces and Surfaces (NIS), University of Turin, Via Pietro Giuria 7, 10125 Turin, Italy

**Correspondence:** Roberto Cossio (roberto.cossio@unito.it)

Received: 11 October 2022 – Revised: 20 February 2023 – Accepted: 25 April 2023 – Published: 31 May 2023

**Abstract.** The ultramafic body of Monte Avic (Aosta Valley, Western Alps, Italy) consists of antigorite serpentinite and Ti-clinohumite metadunite. They host late metamorphic veins, up to a couple of centimeters thick, compact, and homogeneous, with a "porcelain" appearance. Vein colors range from yellowish to light greenish, light yellowish fading to white, or rare orange. The veins consist of 15-sector PS-15 polygonal serpentine, with chemical composition $Mg_{2.85}$ $Fe_{0.08}$ $Si_{2.05}$ $O_{7.05}$ $[OH]_{3.95}$. Recognition of this unusual phase is supported by diagnostic satellite reflections in the X-ray powder diffraction pattern (e.g., at $d_{obs}$ of 2.502, 2.336, 2.151, and 1.966 Å) TEM images (showing 15-sector polygonal fibers, mostly 200 nm in diameter and a few µm in length, forming a randomly oriented felt) and a µ-Raman wavenumber, matching previous data. This different evidence affords the successful distinction of PS-15 and PS-30, alternatively using TEM images, X-ray powder diffraction, or the low- and high-wavenumber µ-Raman spectra. At Monte Avic, the vein emplacement was accompanied by significant fluid pressure, as suggested by deformation and dismembering of the host rock, with PS-15 grown within isotropic stress microenvironments characterized by fluid-filled voids. Random growth of the mass-fiber polygonal serpentine was favored by low-strain conditions. PS-15 veins formed at the end of the long polyphase Alpine orogenic evolution, with hydrous fluids possibly deriving from serpentinite dehydration in the depth.

## 1 Introduction

This report follows previous studies on the vein minerals of ultramafics of Piemonte and Aosta Valley in the Western Alps (Belluso et al., 1994; Alberico et al., 1997; Compagnoni and Groppo, 2006; Groppo et al., 2006; Groppo and Compagnoni, 2007a, b), later focused on the use of micro-Raman spectroscopy as a rapid, reliable technique for the identification of serpentine minerals (Groppo et al., 2006). During a preliminary field survey in the Monte Avic area, a new type of serpentine vein was discovered in three localities and identified by this study as characterized by dominant PS-15 polygonal serpentine.

PS-15 constitutes just one step of the complex serpentine structural hierarchy, arising from the different ways in which basic Mg–O octahedra and Si–O tetrahedra assemble together. They form flat layers in lizardite (Liz), curled layers in chrysotile (Ctl), alternating layers in antigorite (Atg), flat kinked layers in polygonal serpentine (PS), and flat geodesically kinked layers in polyhedral serpentine (PHS) (Mellini, 2013, and references therein). In particular, polygonal ser-

pentines represent special polytypic arrangements, characterized by a fixed number of lizardite sectors (15 or 30 in PS-15 and PS-30, respectively), where concerted polytypic variation occurs from sector to sector, giving rise to a polytypic kaleidoscope (e.g., Baronnet and Devouard, 2005; Mugnaioli et al., 2007). Baronnet et al. (1994) and Baronnet and Devouard (1996) explained the occurrence of the two different PS variants and proposed that the magic numbers 15 and 30 were determined by the occurrence of partial dislocations of +b/3 or +b/6 from layer to layer (equivalent to five b periodicities added at each turn). One of the implications for the model was the intersector cyclic distribution of twins and/or different polytypes. Polygonal serpentine may therefore be defined as a cyclic twin, based on the lizardite structure, but with fixed numbers of sectors (15 or 30) within one turn. Last but not least, these arrangements give rise to a non-crystallographic local fivefold symmetry (Cressey et al., 2010).

Although not always sharply identified, polygonal serpentine has been present in the mineralogical literature for a long time (e.g., the several references collected in Mellini, 2013). Among others, Varlakov (1984) defined polygonal serpentine as a variety transitional between lizardite and clinochrysotile; Mellini (1986) published transmission electron microscopy (TEM) images of polygonal serpentine within the slip veins of the Balangero serpentinite, where chrysotile replaces balangeroite but is later transformed to polygonal serpentine. Major problems dealing with polygonal serpentine have been represented by the difficult accurate identification, further complicated by the possible intermixture of several phases (PS-15, PS-30, and chrysotile, all of them often present in a lizardite or antigorite matrix). Apparently, up to now for many authors only TEM seemed appropriate for this goal. As far as the PS recognition goes, it remains difficult, and any attempt to determine the accurate phase relationships may be in vain.

By this note we report data for an almost pure PS-15 occurrence. Hopefully, this may extend the possibilities for successful PS identification, as well as discriminate PS-15 from PS-30. The acquisition of this and other future PS specimens may finally offer a well-constrained strong base, useful for better appraisal of reaction mechanisms and phase relationships (for instance, why PS-15 and why PS-30; what is the mechanism of replacement of chrysotile by PS; and what is the role of $P$, $T$, local stress fields, fluid pressure, etc.?).

## 2 Geological framework of the Monte Avic Massif

The Monte Avic Massif, one of the largest ultramafic bodies of the Western Alps, is exposed in the middle Aosta Valley for an area of ca. 180 km$^2$ (Fig. 1).

According to the explanatory notes of Sheet 091 (Châtillon) of the 1 : 50 000 geological map (Dal Piaz et al., 2010), the Monte Avic Massif consists of serpentinized peridotites, rich in Ti-clinohumite, olivine, diopside, and magnetite, with frequent intercalations of magnetite-bearing chlorite schist, and is surrounded by a thick layer of ophicarbonatic rocks, at least in a part of possible sedimentary origin (Tartarotti et al., 1998). Within this complex geological context, the three yellow stars in Fig. 1b identify the sampling sites of this study.

Through new geological field observations in the massif we noticed the presence of two main types of ultramafics, which can easily be distinguished on the basis of their colors: (i) a greenish type that mainly consists of antigorite, hereinafter referred to as antigorite serpentinite, and (ii) an ochre type, mainly consisting of metamorphic olivine, referred to as "metadunite" (see Sect. 4.1) because the olivine is not a relic of the original mantle protolith but a prograde metamorphic mineral formed during the subduction phase of the Alpine orogeny. The two lithotypes occur as alternating layers several meters thick, showing gradual transitions between them, with the antigorite serpentinite forming later at the expense of the metadunite.

## 3 Experimental

Several techniques concurred to define the nature of the Monte Avic specimens (i.e., optics, scanning electron microscopy coupled with energy dispersive spectrometry (SEM/EDS), X-ray powder diffraction data (XRPD), TEM, micro-Raman (μ-R), hardness testing) and offered data useful for approaching the still pending problems.

The petrographic study was carried out on a representative rock sample from which three polished thin sections (30 μm thick) were prepared. Thin sections were examined by means of a ZEISS WL polarized light microscope, and photomicrographs were taken with an Olympus BX41-P polarized light microscope equipped with a digital camera.

Scanning electron microscopy coupled with energy dispersive spectrometry (SEM/EDS) was done using a JEOL IT300LV, equipped with an AZtec Oxford analyzer and an SDD XACT3 detector. Data were acquired at 15 kV acceleration voltage, with a 5 nA probe and count rate of $10^5$ cp s$^{-1}$.

X-ray powder diffraction data (XRPD) were acquired from the Department of Earth Sciences of the University of Turin by means of a high-resolution X-ray diffractometer Rigaku SmartLab® XE, with Cu$K\alpha$ radiation. The measurements on powder specimens were carried out in Bragg–Brentano geometry, using an automatic zero sample alignment procedure. To improve the resolution, acquisitions were made using a 2.5° Soller slit on the primary beam and a 0.5° Soller slit on the diffracted beam, for about 15 h and with steps of 0.001°. The choice of two different Soller slits reduced the very slight asymmetry of the most intense peaks lower than about 25° 2$\theta$. Microarea XRPD was performed over a polished rock slab, using a cross beam optics (CBOs) multilayer mirror, working in parallel beam (PB) conditions and coupled to a CBO-f unit to convert the line focus to a point focus.

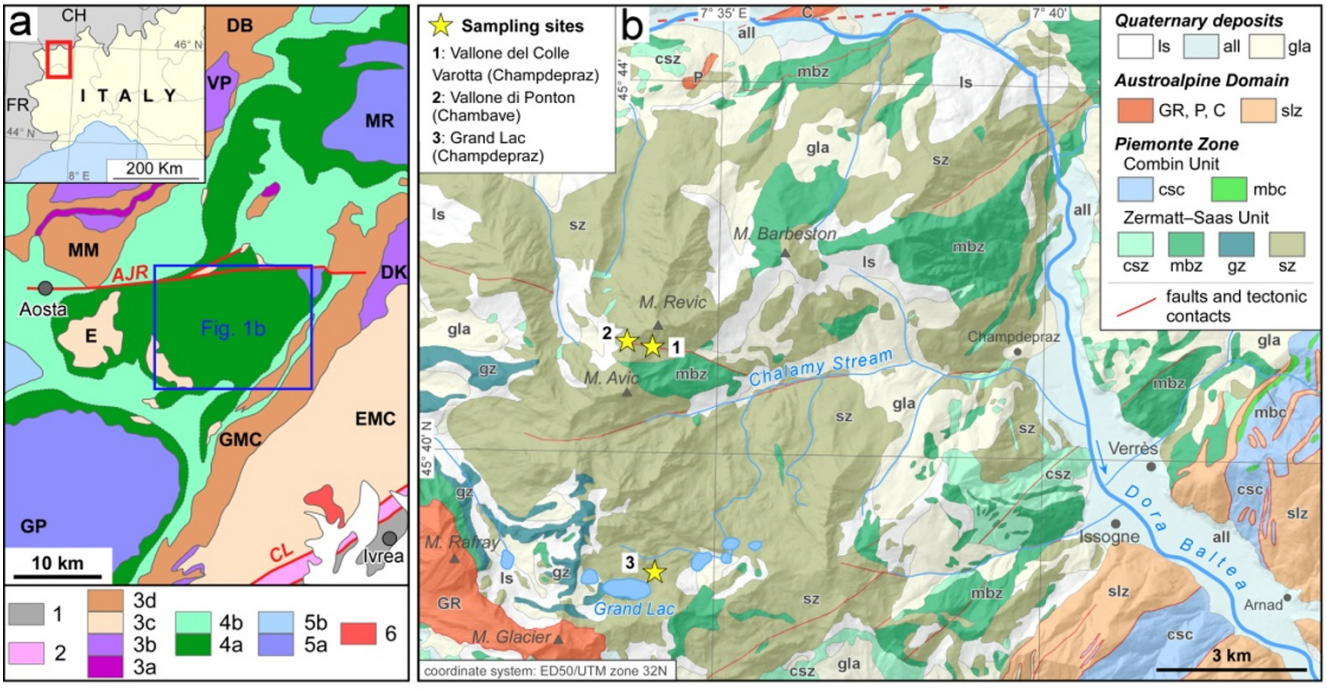


**Figure 1.** **(a)** Tectonic sketch map of the northwestern Alps and its geographic location in NW Italy (modified from Bigi et al., 1990). (1) *South Alpine system*, undifferentiated. (2) *Canavese zone*. (3) *Austroalpine system*: (3a) Roisan and Mt. Dolin Mesozoic cover and undifferentiated mylonites, (3b) units with prevailing amphibolite- to granulite-facies pre-Alpine overprint (Valpelline series: VP, second diorite–kinzigite zone: DK), (3c) units with Alpine eclogite-facies overprint (eclogitic micaschist complex of the Sesia zone: EMC, Mt. Emilius unit: E), and (3d) units lacking Alpine eclogite-facies overprint (Gneiss Minuti Complex of the Sesia zone: GMC, thrust sheets of Dent Blanche and M. Mary: DB, MM). (4–6) Penninic zone. (4) *Piemonte zone*: (4a) units related to the eclogite-facies Zermatt–Saas zone and corresponding units south of the Dora Baltea River and (4b) units related to the epidote blueschist-facies Combin zone. (5a) *Upper Penninic units* with Alpine eclogite-facies overprint (Gran Paradiso: GP, Monte Rosa, MR). (5b) Intermediate Penninic units with Alpine epidote blueschist-facies overprint (*Gran San Bernardo nappe*). (6) *Oligocene plutonic rocks*. Main tectonic lineaments (in red): Canavese line: CL, Aosta-Colle di Joux-Colle della Ranzola fault system: AJR. **(b)** Geological scheme of the Monte Avic area, middle Val d'Aosta (geological boundaries after De Giusti et al., 2003; hillshade: Arpa Piemonte, Sfumo_Europa_WM). Abbreviations: slope deposits and landslides, ls; alluvial deposits, all; glacial deposits, gla; Glacier–Rafray unit, GR; Pontey unit, P; Châtillon–St. Vincent Unit, C; Sesia–Lanzo zone, slz; *Combin unit* (calc-schist: csc; metabasite: mbc); *Zermatt–Saas unit* (calc-schist: csz; metabasite, amphibolite, and minor eclogite: mbz; metagabbro: gz; serpentinite including meta-ophicarbonatic rocks: sz). The dashed line at the extreme top edge of the map is the trace of the Aosta-Colle di Joux-Colle della Ranzola fault system, trending ca. E–W.

A 2 mm limiting slit was used to select the area, with the massive sample mounted on a motorized 4 in. wafer plate. Data were collected using a HyPix-3000 2D semiconductor X-ray detector in vertical orientation and 2D mode to maximize diffracted intensities. The microarea XRPD pattern was collected using Cu$K\alpha$ radiation, operating at 40 kV and 30 mA, in the range 3–85° $2\theta$, with a step size of 0.001° at a rate of 0.1° per step, thus resulting in smooth, almost noise-free data.

Transmission electron microscopy (TEM) investigation was performed by a JEOL JEM-2100P at the platform of microscopy of the University of Milano-Bicocca. The instrument operates at 200 kV and is equipped with an Oxford EDS spectrometer for elemental analysis and a Gatan Rio CMOS camera for image acquisition. Images were taken in bright field and high-resolution modes at magnifications between 15 and 300 kX. Samples were prepared by ion milling 3 mm wide disks, selected on a double polished petrographic thin section, using a Gatan PIPS II cool instrument. Before removing the disk and ion milling, a 3 mm wide Cu ring with an internal hole of 1 mm was glued on the area of interest. TEM mounts were coated with 20 nm of carbon to avoid electrostatic charging during observations.

Micro-Raman spectra (μ-R) were acquired from the Department of Earth Sciences of the University of Turin, using a Horiba Jobin Yvon HR800 LabRAM spectrometer equipped with a Nd:YAG green laser (532 nm) in N–S polarized mode, delivering 8 mW on the sample; an Olympus BX40 optical microscope; and a charge-coupled device (CCD) detector cooled to −70 °C by the Peltier effect. The analytical conditions were a 200 μm confocal hole, 100× objective (1 μm lateral spatial resolution), and 1 $cm^{-1}$ spectral resolution with

a 600 grooves $mm^{-1}$ grating. Measurements were done on polished thin sections. The spectrometer was calibrated with silicon standard (520.7 $cm^{-1}$). The acquisition time was 10 s with 10 accumulations per spot. Spectra were processed using the LabSpec 5 acquisition software.

Hardness was determined by a micro Vickers hardness tester from Buehler, loaded with 100 g, located at the Department of Chemistry, University of Turin. In total 15 measurements have been performed on a polished rock slab about 0.5 cm thick.

The selection of samples for the different analyses was based upon careful study of the optical thin sections. These were used to extract well-defined TEM mounts and to collect several localized μ-R spectra (more than 200). XRPD patterns were repeated using both standard powder preparation and focused microdiffraction over rock slabs. All the different data were constantly consistent, significantly suggesting the homogeneous nature of the investigated sample.

## 4 Vein appearance at meso- and micro-scale and petrography

Serpentine veins were found above 2500 m a.s.l. in loose blocks of the talus between Monte Avic and Monte Revic (Fig. 1b, sites 1 and 2) and near the Grand Lac (Fig. 1b, site 3). At the three sites, the vein-bearing blocks derive from the highest and inaccessible parts of the overlying vertical valley walls. Vein thickness ranges from a few millimeters to about 2 cm, and the infilling material is compact and homogeneous, with an unusual porcelain appearance (Fig. 2). The color on the weathered surface is mostly yellowish to light greenish (Fig. 2a and b); locally, light yellowish fading to white (Fig. 2c); or more rarely orange colors also occur. On the fresh cut, the vein color is yellow (Fig. 3). One representative sample, greenish in color on weathered surface but yellow on the fresh cut (Fig. 2a), was collected from a loose block at site 1 (sample Monte Avic 1). It consists of two veins (MA 1a and MA 1b) cutting across an ochre-colored ultramafic rock, mainly composed of olivine.

### Sample Monte Avic 1

The host rock is surrounded by two yellow veins (Fig. 3). Three polished thin sections were made (Fig. 3); OF4112/1 samples the left vein (MA 1a) and its reaction zone with the host rock, OF4112/2 the host rock only, and OF4112/3 the right vein (MA 1b) and its reaction zone.

The vein/host rock contact may be roughly straight, such as in the left vein MA 1a, or more complex, such as in the right vein MA 1b. Close to the contact, fragments of the host rock are commonly embedded in the vein. In both veins, the reaction zones are about 1 cm thick, with evident mineralogical banding (Fig. 3).

### 4.1 The host ultramafic rock (OF4112/2)

The complex tectono-metamorphic evolution of this rock will be only briefly summarized here because it is irrelevant to the evolution of the late PS-15 veins and is detailed elsewhere.

The host ultramafic rock, which consists of the stable mineral assemblage olivine (Ol with $Fo_{>95}$), minor magnetite (Mt), antigorite (Atg), little Mg-chlorite (Mg-Chl), and rare titanian hydroxyl-clinohumite (Ti-Chu), is classified as a metadunite. The mineral assemblage indicates eclogite-facies conditions in the range 500–600 °C, consistent with the early Alpine HP-peak metamorphic conditions estimated for most of the Zermatt–Saas zone (e.g., Dal Piaz et al., 2010, and references therein). The microstructural relationships clearly show that olivine crystals contain a folded foliation defined by magnetite alignments. While this stable assemblage of olivine (forsterite-rich, $Fo_{>95}$) with Mt on the one hand excludes this olivine as the original mantle one, on the other hand it implies that the mantle protolith has undergone an important hydration process (earlier than the eclogite-facies metamorphism) that converted the mantle peridotite into a serpentinite. The later evolution is especially evident at the transition zone between the two interlayered ultramafic types, where a new hydration event mainly localized along shear planes converted the eclogite-facies metadunite into a greenschist-facies antigorite serpentinite.

In conclusion, the Monte Avic ultramafics record a long-lasting tectono-metamorphic history implying the earliest (most likely ocean floor) pervasive serpentinization, followed by a typical orogenic evolution characterized by an initial high-$P$ metamorphism related to subduction and overprinted by a later greenschist-facies event connected to the exhumation.

The studied metadunite between the two PS-15 veins (Fig. 3) further shows a network of veinlets (a few tens of μm thick) roughly parallel to the main rock foliation where olivine is replaced by lizardite ± brucite ± magnetite (Fig. 4), according to the reaction

$$\text{olivine} + \text{water} \rightarrow \text{lizardite} + \text{brucite} \pm (\text{magnetite} + \text{hydrogen}).$$

### 4.2 The veins and their reaction zones (OF4112/1 and OF4112/3)

At the contact with the host rock, the light-yellow veins MA 1a and MA 1b exhibit reaction zones similar in thickness, microstructure, and mineralogy. Starting from the contact, the reaction zones consist of at least three layers. In the first layer, darker for the higher-magnetite content, the olivine is gradually replaced by lizardite + magnetite (Fig. 5) ± brucite (identified mostly by μ-R). The second lighter layer mostly consists of brucite porphyroblasts (Br; Fig. 5), locally intergrown with fine-grained lizardite, which may include magnetite.

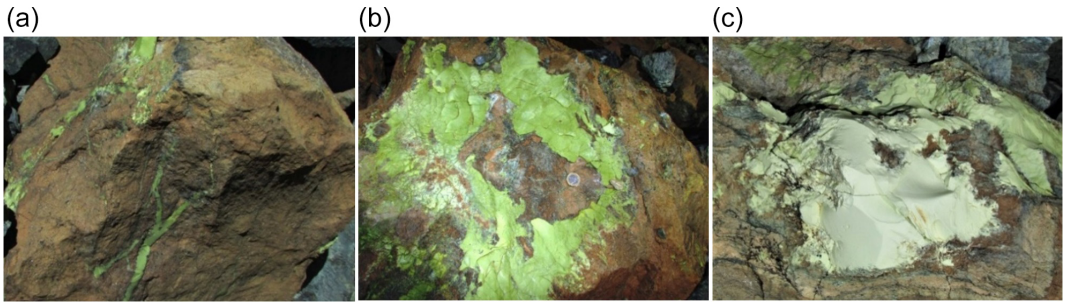


**Figure 2.** Field appearance of the Monte Avic veins, perpendicular **(a)** and roughly parallel **(b, c)** to vein selvages, respectively. From **(a)** to **(c)**, fields of views are ca. 55, 30, and 25 cm, respectively.

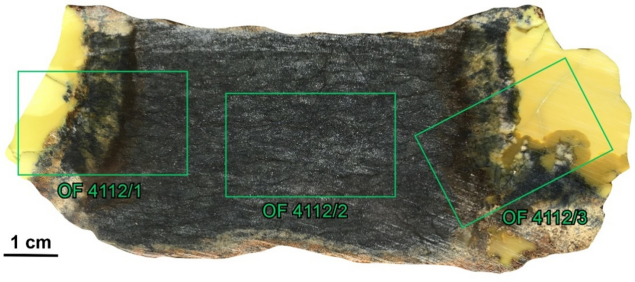


**Figure 3.** Polished slab of sample Monte Avic 1 with locations of the three thin section sites. OF4112/1 includes the left vein (MA 1a), reaction zone, and host rock; OF4112/2 only host rock; and OF4112/3 right vein (MA 1b). The reaction zones are further subdivided in layers characterized by a different microstructure and mineralogy.

Towards the vein contact, a third discontinuous dark layer occurs, which is rich in coarser-grained euhedral magnetite embedded in a lizardite matrix.

The vein consists of a homogeneous, almost isotropic colorless or beige-colored matter, eventually coming out to be polygonal serpentine. PS not only fills the vein but also penetrates and dismembers the rock, which mainly consists of relict antigorite and magnetite (Fig. 6).

The chemical composition of the polygonal serpentine was determined by SEM/EDS, analyzing two carefully selected rectangular arrays ($660 \times 450\,\mu m$ wide), each of them producing 300 spot analyses (step size of $30\,\mu m$). Both the regions yield constant, homogeneous, and common results, with standard deviations on major elements (magnesium and silicon) of 0.6 % and 0.2 %, respectively. The Monte Avic PS serpentine is chemically homogeneous and constant, with formula

$$Mg_{2.85}\,Fe_{0.08}\,Si_{2.05}\,O_{7.05}\,[OH]_{3.95}.$$

## 5 X-ray powder diffraction (XRPD)

Mugnaioli et al. (2007, Fig. 13) reported that the XRPD pattern of PS-30 polygonal serpentine (previously determined by TEM) exhibits additional reflections in the 18–24° $2\theta$ interval, not present in chrysotile and other serpentine minerals. Therefore, we performed new X-ray acquisitions on their S491 highest-crystallinity sample and compared it with the present data from the Monte Avic veins. The patterns are reported in Fig. 7, and the observed interplanar distance ($d_{obs}$) and peak intensity ($I/I_0$) values are listed in Table 1, together with data by Mugnaioli et al. (2007, Fig. 13). We also extended our XRPD investigation to their sample S1279, described (again by TEM) as mostly consisting of PS-15. The Monte Avic samples produced undistinguishable XRPD data from both the usual powder sample and the focused microdiffraction experiment; this coincidence indicates the absence of PS-preferred orientation.

Characteristic features of the XRPD patterns of polygonal serpentines are additional satellite reflections close to 20 and 40° $2\theta$ (Fig. 7 and Table 1). Similar reflections have also been reported for other polygonal serpentines (e.g., Morandi and Felice, 1979; Varlakov, 1984; Logar, 1992), initially interpreted as due to the presence of multilayer lizardite polytypes.

Whereas the three patterns indicate that all the samples are polygonal serpentines, significant differences affect the additional satellite reflections, clustered close to 20 or 40° $2\theta$ (Fig. 7): namely, PS-15 and PS-30 have their own different characteristic clusters of satellites (see Table 1 and Fig. 7). More specifically, OF4112 matches the S1279 pattern, in particular in the 35–45° range, the most significant reflections ($d_{obs}$) being at 2.502, 2.336, 2.151, and 1.966 Å. Conversely, this cluster is absent in PS-30, or, more simply, the medium-intensity peak close to 2.45 Å in PS-30 replaces the strong peak close to 2.50 Å in PS-15. The higher intensities of OF4112 with respect to S1279 suggest better crystallinity, as confirmed by the following TEM images (see Sect. 6). Small differences in the intensities of the same peaks may depend on different preferential orientations of the fibers. Furthermore, the comparison among the different

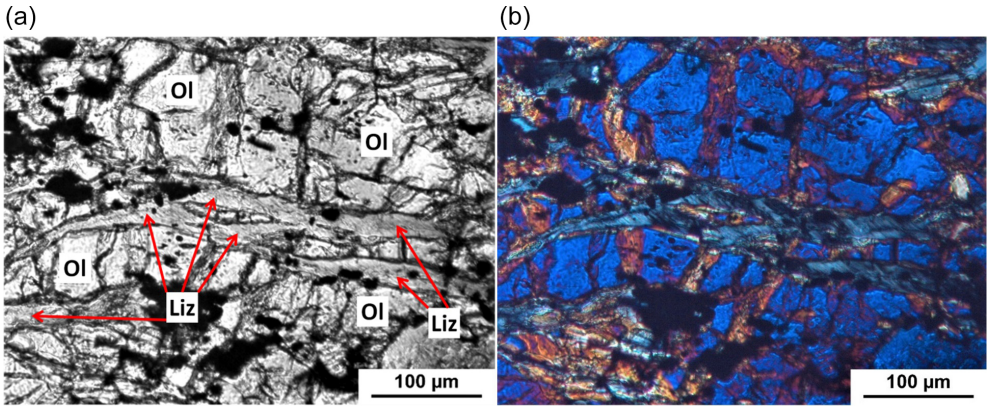


**Figure 4.** The host rock is crossed by a subparallel network of thin veinlets where olivine (Ol) is altered to lizardite (Liz) and rare brucite (mostly identified by µ-R) ± magnetite (black). **(a)** PPL and **(b)** XP. OF4112/2.

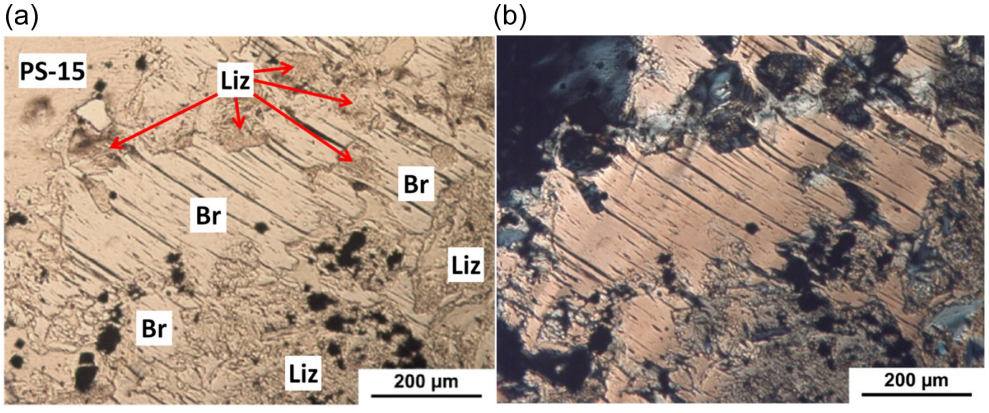


**Figure 5.** Reaction zone. A brucite porphyroblast (Br) includes aggregates of lizardite (Liz) and magnetite (opaque grains, lower side). PPL **(a)** and XP **(b)**. OF4112/3.

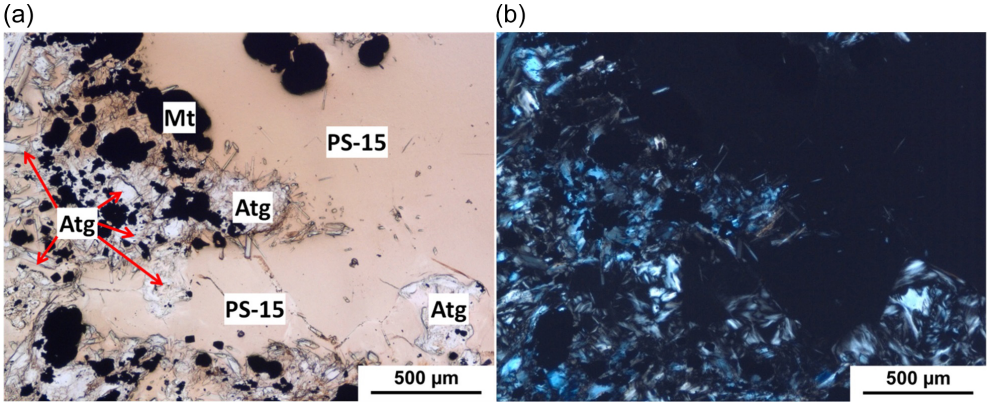


**Figure 6.** Host rock/vein contact. **(a)** The polygonal serpentine vein (PS-15, beige colored) is permeating and dismembering the host rock that close to the vein selvages is mainly consisting of relict antigorite (Atg, white) and old + new magnetite (Mt, black). **(b)** The PS-15 vein is black because isotropic under crossed polars. In the host rock, only the antigorite flakes are evident. PPL **(a)** and XP **(b)**. OF4112/3.

**Table 1.** X-ray powder diffraction patterns ($d_{obs}$ in Å and $I/I_0$) of the Monte Avic vein polygonal serpentine (OF4112) compared to the original data of S491 by Mugnaioli et al. (2007) and new measurements of S491 (PS-30) and S1279 (PS-15). See Fig. 7.

| OF4112 PS-15 (this paper) | | S491 PS-30 (this paper) | | S491 PS-30 (Mugnaioli et al., 2007) | | S1279 PS-15 (this paper) | |
|---|---|---|---|---|---|---|---|
| $d_{obs}$ | $I/I_0$ | $d_{obs}$ | $I/I_0$ | $d_{obs}$ | $I/I_0$ | $d_{obs}$ | $I/I_0$ |
| 7.296 | 100 | 7.317 | 100 | 7.338 | 100 | 7.300 | 100 |
| | | | | 4.613 | 6 | | |
| 4.595 | 22 | 4.588 | 7 | 4.586 | 6 | 4.593 | 12 |
| 4.526 | 14 | | | 4.536 | 5 | 4.543 | 13 |
| | | 4.518 | 5 | | | | |
| 4.416 | 9 | 4.404 | 3 | 4.415 | 4 | 4.402 | 5 |
| 4.258 | 7 | 4.250 | 2 | 4.264 | 3 | 4.260 | 3 |
| | | 4.212 | 1 | | | | |
| 4.085 | 5 | 4.082 | 2 | 4.094 | 3 | 4.078 | 1 |
| 3.903 | 4 | 3.902 | 1 | 3.908 | 2 | 3.899 | 2 |
| 3.643 | 59 | 3.657 | 32 | 3.660 | 59 | 3.660 | 25 |
| 3.524 | 2 | 3.529 | 1 | 3.529 | 2 | | |
| 3.346 | 2 | 3.346 | 1 | 3.360 | 2 | 3.343 | 1 |
| 3.173 | 1 | 3.177 | 1 | 3.182 | 1 | 3.172 | 1 |
| 3.012 | 1 | 3.017 | 1 | 3.021 | 1 | 3.013 | 1 |
| 2.859 | 1 | | | 2.866 | 1 | 2.854 | 1 |
| | | | | 2.729 | 1 | | |
| 2.659 | 3 | 2.650 | 2 | 2.661 | 2 | 2.660 | 2 |
| 2.622 | 10 | | | | | 2.619 | 9 |
| 2.589 | 2 | 2.586 | 3 | 2.590 | 5 | | |
| | | 2.545 | 3 | 2.550 | 5 | | |
| 2.502 | 66 | | | | | 2.500 | 57 |
| | | 2.449 | 13 | 2.455 | 19 | | |
| 2.428 | 4 | | | | | 2.430 | 3 |
| | | | | | | 2.345 | 3 |
| 2.336 | 14 | | | | | 2.335 | 15 |
| | | 2.275 | 2 | 2.279 | 3 | | |
| | | 2.212 | 1 | 2.217 | 2 | | |
| 2.151 | 13 | | | 2.158 | 1 | 2.150 | 9 |
| 2.093 | 3 | 2.090 | 4 | 2.093 | 5 | | |
| | | | | 2.088 | 4 | | |
| | | 2.028 | < 1 | 2.030 | 1 | | |
| 1.966 | 16 | | | | | 1.966 | 12 |
| | | 1.909 | 1 | 1.912 | 1 | | |
| | | 1.851 | 1 | 1.855 | 1 | | |
| 1.823 | 2 | 1.828 | 1 | 1.829 | 1 | 1.822 | 1 |
| 1.794 | 3 | | | | | 1.794 | 2 |
| 1.741 | 3 | 1.743 | 3 | 1.747 | 4 | 1.738 | 2 |
| | | | | | | 1.724 | 1 |
| | | | | | | 1.702 | 1 |
| 1.640 | 7 | | | | | 1.639 | 5 |
| | | 1.594 | 1 | 1.598 | 1 | | |
| | | 1.547 | 2 | 1.551 | 4 | | |
| 1.537 | 23 | 1.537 | 5 | 1.538 | 10 | 1.537 | 16 |
| 1.504 | 13 | 1.504 | 2 | 1.505 | 3 | 1.503 | 8 |
| 1.461 | 1 | 1.463 | 1 | 1.463 | 2 | 1.457 | 1 |
| | | 1.425 | 1 | 1.424 | 1 | | |
| 1.416 | 3 | 1.416 | 1 | 1.416 | 1 | 1.415 | 2 |

**Table 1.** Continued.

| OF4112 PS-15 (this paper) | | S491 PS-30 (this paper) | | S491 PS-30 (Mugnaioli et al., 2007) | | S1279 PS-15 (this paper) | |
|---|---|---|---|---|---|---|---|
| $d_{obs}$ | $I/I_0$ | $d_{obs}$ | $I/I_0$ | $d_{obs}$ | $I/I_0$ | $d_{obs}$ | $I/I_0$ |
| 1.384 | 3 | | | | | 1.384 | 2 |
| 1.327 | 2 | | | | | 1.328 | 1 |
| 1.311 | 9 | 1.315 | 2 | | | 1.309 | 7 |
| | | 1.300 | 1 | | | | |
| 1.280 | 3 | | | | | 1.280 | 3 |
| | | | | | | 1.253 | < 1 |
| 1.212 | 2 | 1.218 | < 1 | | | 1.211 | 1 |
| 1.186 | 1 | | | | | 1.185 | < 1 |
| 1.169 | 1 | | | | | 1.168 | 1 |
| | | 1.153 | < 1 | | | | |
| 1.122 | 1 | | | | | 1.121 | 1 |
| 1.076 | 1 | | | | | 1.075 | 1 |
| | | 1.088 | < 1 | | | | |
| 1.058 | 2 | 1.058 | 1 | | | 1.056 | 1 |
| | | 1.044 | < 1 | | | | |
| 1.038 | < 1 | | | | | 1.029 | < 1 |

patterns indicates that each PS-15 sample may also contain minor amounts of PS-30 and PS-30 minor amounts of PS-15, respectively.

## 6 Transmission electron microscopy (TEM)

The TEM images were obtained from selected regions of the petrographic thin sections, cross-related to their XRPD and Raman characterizations. They show that the MA veins consist of a felt of mass-fiber polygonal serpentine, randomly oriented and associated with minor, large, and acicular antigorite fibers (Fig. 8b), as well as with rare chrysotile. Each PS fiber, cut normal to elongation, shows the typical scroll-like structure with 15 polygonally arranged sectors (PS-15). The average PS-15 fiber cross-diameter is about 200 nm, while the fiber length is several µm. Most fibers lack the central hole or have a very small circular hole in the core (Fig. 9a and b). The average fiber cross-diameter of chrysotile is about 30–35 nm, with a circular hole in the core less than 10 nm across. In the felt, fibers are surrounded by empty space, most likely originally filled by the hydrous fluid phase. No PS-30 was observed during the TEM sessions. The number of PS-15 fibers observed during the TEM sessions may be estimated in the order of some thousands and corresponds to a volume of order of magnitude larger than the Ctl volume.

## 7 Micro-Raman spectroscopy

µ-Raman spectroscopy is useful for the identification of serpentine minerals (e.g., Petriglieri et al., 2015; Rooney et al., 2018; Compagnoni et al., 2021). However, Tarling et al. (2018) were skeptical about the possibility of distinguishing polygonal serpentines from lizardite on a µ-Raman base only. In what follows, we further explore this apparently still unsettled topic.

Homogeneity of the vein material was checked by single spectra and spectral profiles (at steps of 0.5 µm), performed at random points in the two veins, for a total of over 200 µ-R spectra. All the spectra resulted in very similar peak positions and intensities (thus overcoming the relevant µ-R anisotropy observed in oriented crystals by Compagnoni et al., 2021, and Tarling et al., 2022). In particular, the standard deviation from the mean value curve is very low; the $+1\sigma$ and $-1\sigma$ curves obtained by summing all the Raman spectra channel by channel tightly bracket and practically overlap the mean curve. Therefore, we conclude that each point of the vein contains fibers present in all directions; this is because, being the volume sampled by the Raman laser at least 2 or 3 orders of magnitude larger than the individual serpentine fibers, Raman spectra results are very similar, or even identical, if the fibers are randomly oriented in any direction (as indicated by TEM images, too). Consequently, just one representative spectrum, labeled OF4112, will be discussed.

The OF4112 representative spectrum was deconvolved using the fitting procedure illustrated by Compagnoni et al. (2021). Frequencies are reported in Fig. 10 for the low-

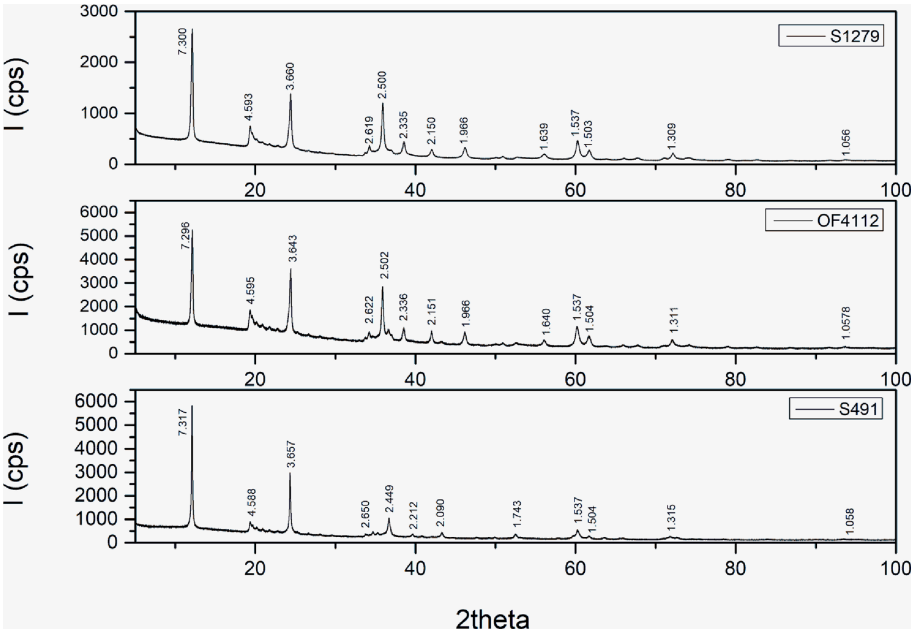


**Figure 7.** XRPD patterns in the range 10 to 100° $2\theta$ of samples S1279 (PS-15) and S491 (PS-30) of Mugnaioli et al. (2007) compared with the Monte Avic sample (OF4112). In all the patterns, the clusters of additional satellite reflections are typical of polygonal serpentine. The OF4112 pattern, which overlaps that of S1279, confirms its PS-15 nature.

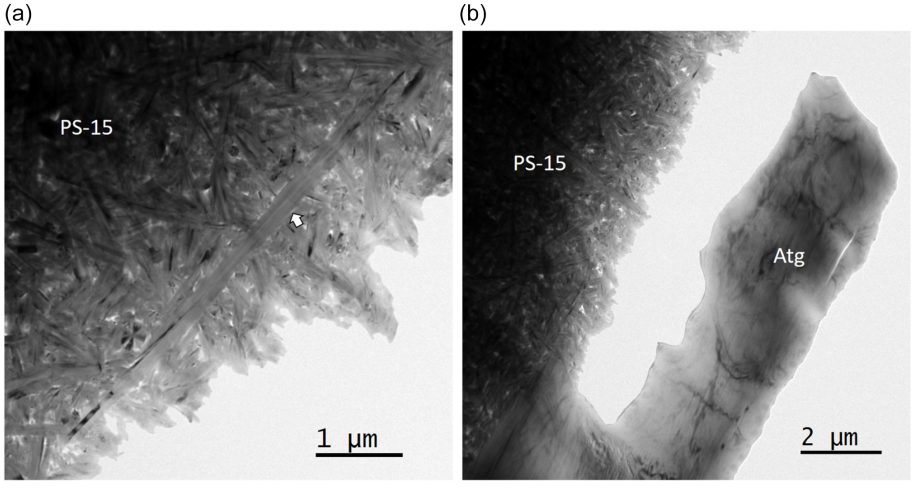


**Figure 8.** Low-magnification TEM images of serpentine from the Monte Avic ultramafite. **(a)** Bright field image showing a felt of polygonal serpentine fibers, randomly oriented and separated by voids. Note the long PS fiber running diagonally at the center of the image (arrow). **(b)** Large antigorite single crystal (Atg) embedded in the polygonal serpentine felt.

wavenumber (100–1200 $cm^{-1}$) and in Fig. 11 for the high-wavenumber region (3600–3750 $cm^{-1}$); in both figures the red line is the result of the deconvolution peaks (in color) of the experimental curve (in black). Note the high overlap of the two red and black curves.

Wavenumber and peak shapes match the observations reported by Compagnoni et al. (2021) for the oriented sections of the S1283 specimen (mostly consisting of PS-15, with rare PS-30). The major benefit of OF4112 now derives from its complete XRPD and TEM characterization, indicating the absence of PS-30 and chrysotile. Therefore, at present, the current µ-R Monte Avic data most probably constitute the best PS-15 reference, in particular for µ-R studies of isotropic veins with no preferred orientation. A minor difference affects overall intensities, in OF4112 spectra 40 %–50 % lower than in the oriented S1283, due to textural features (in particular, the lower number of crystals cut parallel to *c*, recalling the explanation previously given by Compagnoni et

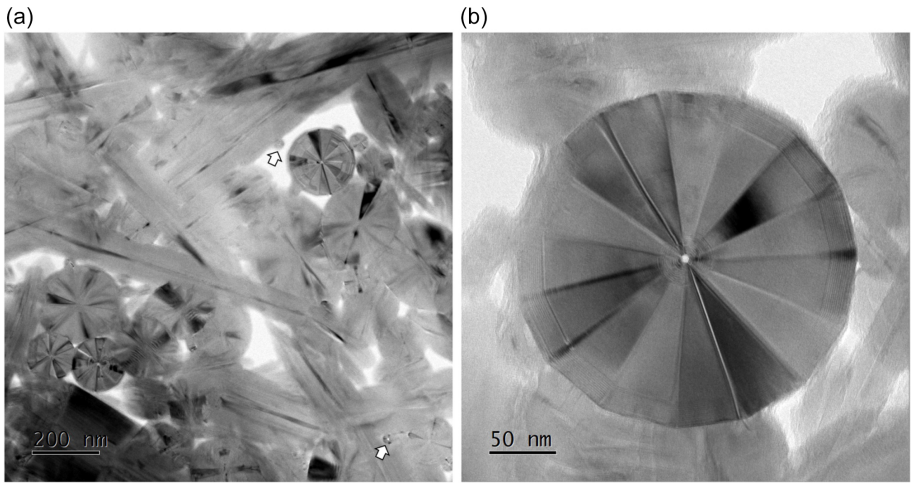


**Figure 9.** TEM images of Monte Avic PS-15. **(a)** Bright field image showing cross and longitudinal sections of polygonal serpentine fibers separated by voids. Sparse, small chrysotile fibers are also present (arrows). **(b)** Lattice fringe image of a cross section of a 15-sector PS fiber.

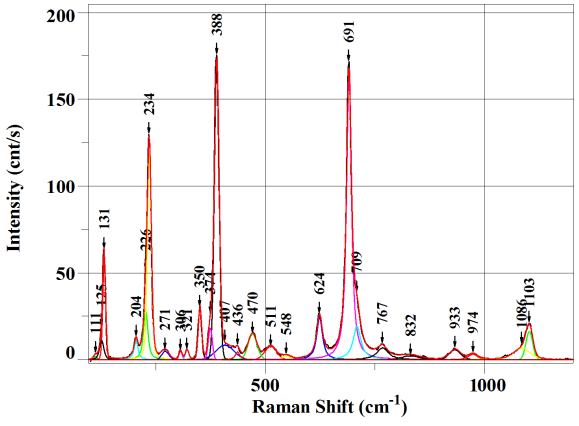


**Figure 10.** μ-R representative spectrum of OF4112 in the low-wavenumber (100–1200 $cm^{-1}$) region. See the text for an explanation of the different colors.

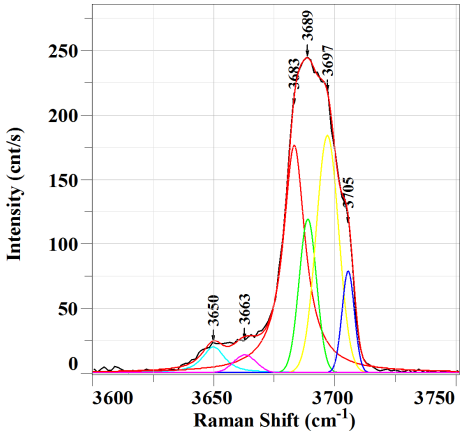


**Figure 11.** μ-R representative spectrum of OF4112 in the high-wavenumber (3600–3750 $cm^{-1}$) region. See the text for an explanation of the different colors.

al., 2021). In the low-wavenumber region (Fig. 10), being the OF4112 μ-R spectrum merged over all the fiber orientations, we further support its identification by frequency comparison with the arithmetic mean of the three different orientations of fibrous serpentines (Ctl, PS-30, and PS-15; Compagnoni et al., 2021), selectively summarized in our Table 2. Root mean square (RMS) differences calculated for the low-wavenumber region give consistent and reliable results because the deconvolution is simple, peaks being usually single. The comparison of RMS values shows that the best match exists between OF4122 and PS-15 (Table 2).

In the high-wavenumber region (Fig. 11), the overall shape of the large band is characterized by two shoulders on the right side of the main peak. In the most interesting portion, between 3670 and 3710 $cm^{-1}$, four bands are obtained from the best deconvolution procedure, whose frequencies ($b1 = 3683 \pm 1\,cm^{-1}$, $b2 = 3689 \pm 1\,cm^{-1}$, $b3 = 3697 \pm 1\,cm^{-1}$, $b4 = 3705 \pm 1\,cm^{-1}$) are similar to both PS-15 and PS-30. However, the two polygonal serpentines can be distinguished because the peak intensities are systematically different (Compagnoni et al., 2021): b1 dominates in PS-30, while b3 in PS-15 (see Fig. 11). Therefore, the μ-Raman spectrum also indicates that OF4112 is a PS-15 polygonal serpentine.

## 8 Overall hardness (Hv)

Due to its massive porcelain appearance and the homogeneity of the veins, used by mineral collectors and semi-precious-stone cutters to make ornamental objects such as "cabochon", we thought it would be useful to determine their overall hardness.

**Table 2.** Comparison among the fibrous serpentines and OF4112. For chrysotile, PS-30, and PS-15, arithmetic mean values (mean) of the main peak frequencies in the low-wavenumber region from the three main orientations are reported (from Compagnoni et al., 2021). The most intense peaks are in bold. Root mean square (RMS) represents deviations from the OF4112 spectra.

| Ctl (mean) | PS-30 (mean) | PS-15 (mean) | OF4112 |
|---|---|---|---|
| **130.6** | **127.5** | **130.9** | **131** |
| 201.3 | 200 | 202.2 | 203.9 |
| **232.6** | **229.5** | **233.5** | **234.3** |
| **389.7** | **384** | **389.8** | **388.3** |
| 625.6 | 618.9 | 623.6 | 623.5 |
| **693.7** | **687.3** | **692.2** | **690.7** |
| 707.4 | 704.1 | 706.4 | 709 |
| **1106.4** | 1095.3 | **1104.5** | **1103** |
| **2.22** | **4.79** | **1.45** | **RMS** |

Accurate hardness determination was hampered because just after the impact of the load tip the vein material behaved partly elastically and swelled or modified the extension of the impression. Among all these measurements, only five have been taken into account; they limit overall hardness in the 54–110 Vickers hardness range, roughly corresponding to 2–3 in the Mohs scale. In spite of their limited accuracy, these values convey an important result, offering a quick field criterion, capable of discriminating the polygonal serpentine veins (soft) from the chalcedony veins (hard), notwithstanding their similar appearances in the field.

## 9 Discussion and conclusions

### 9.1 The frequency of polygonal serpentine veins

As far as we know, polygonal serpentine veins from the Western Alps have not been reported so far. As already pointed out by Mugnaioli et al. (2007), the mineralogical relevance of polygonal serpentine has been neglected for a long time "owing to the difficulties in identifying the serpentine minerals before the advent of TEM as a routine tool for mineral investigation". Another reason why the polygonal serpentine is not recognized in the field may be due to its porcelain appearance, more similar to massive lizardite than to fibrous serpentine, and even to chalcedony veins. However, based upon our field experience, we expect that in the near future polygonal serpentine will be reported from many ultramafics, provided that appropriate identification tools are available. In that case, new reports of almost pure PS-15 or PS-30 occurrences might clarify the reasons capable of favoring the formation of one of the two forms; according to Mugnaioli et al. (2007), PS-30 would be energetically favored over the less stable PS-15.

### 9.2 The distinction of PS-15 and PS-30

Of course, PS-15 and PS-30 may be discriminated based upon impressive and convincing TEM images. Unfortunately, TEM techniques are not available everywhere; preparation of serpentine TEM specimens may be difficult, as TEM sessions are both time-consuming and expensive, and skilled operators are required. Therefore, simpler approaches would be welcome.

One of these may be X-ray powder diffraction, as PS-15 and PS-30 produce satellites, appearing as different, characteristic clusters (see Table 1 and Fig. 7). For instance, PS-15 shows a characteristic cluster of satellites between 35 and 45° 2$\theta$ ($d_{obs}$ of 2.502, 2.336, 2.151, and 1.966 Å) that is absent in PS-30, or, more simply, the medium-intensity peak close to 2.45 Å of PS-30 is replaced by a strong peak close to 2.50 Å in PS-15. These two PS datasets recall previous data by Krstanovic (1997) for the Crni Kamen polygonal serpentine and the so-called "povlenite" from Mount Povlen. The latter shows additional peaks (appearing starred in Table 1 of Krstanovic, 1997) at 2.496, 2.332, 2.148, 1.967, and 1.638 Å, not present in the Crni Kamen specimen: namely, whereas Crni Kamen (same occurrence as S491) matches our XRPD criteria for PS-30, the Mt. Povlen sample would be one more example for PS-15. Mugnaioli et al. (2007) recalculated the diffraction patterns and showed that the PS-30 satellites arise from the polytypic sequences present there; as a consequence, we expect that the different PS-15 satellites are due to different polytypic sequences.

A second tool is offered by μ-Raman spectroscopy. In particular, slight differences occur in the peak positions of the low-wavenumber region (see Table 2); furthermore, different intensity distributions characterize the peaks forming the wide envelope occurring at the high-wavenumber region, with the dominant role of the b1 deconvolution peak at 3683 $cm^{-1}$ in PS-30 and dominant role of b3 deconvolution peak at 3697 $cm^{-1}$ in PS-15.

Whereas Raman anisotropy largely affects the high-wavenumber region, the low-wavenumber region constantly affords useful constraints. For instance, lizardite can be distinguished from the other serpentine minerals by the absence of a clear and unambiguous peak around 1100 $cm^{-1}$. Minor peaks, variable in shape and intensity in the different serpentine minerals, occur around 1100 $cm^{-1}$, as previously highlighted by other researchers (e.g., Compagnoni et al., 2021). In antigorite, the peak, which occurs at 1045 $cm^{-1}$, is very sharp and more intense than in the other serpentines. In polygonal serpentines, the peak is less intense than in Atg but is sharp and located at values a bit higher or lower than 1100 $cm^{-1}$ for PS-15 and PS-30, respectively. In lizardite, the peak, which occurs around ca. 1070 $cm^{-1}$, is low and poorly defined so that a reliable fitting cannot be obtained.

New field investigations may lead to reconnaissance of further polygonal serpentine veins, even in other occurrences. The new data might enforce, or deny, our Raman in-

terpretation, in particular as far as the Raman-phase recognition is concerned. As we are now actively operating in that direction, we expect to come back to this issue in the near future.

### 9.3 The vein formation conditions

Prior to the vein formation, the metadunite hosting the PS-15 veins consisted of the stable assemblage olivine (Fo $\geq$ 95) – antigorite – magnetite – titanian hydroxyl-clinohumite – Mg-rich chlorite. The antigorite-forsterite stable coexistence constrains $T$ between 450 and 600 °C (Evans and Trommsdorff, 1970), as shown by reactions essentially $T$ dependent. Therefore, a similar $T$ range, at the high-$P$ conditions of the eclogite facies, can be envisaged, in agreement with both the presence of Ti-clinohumite and the Alpine H$P$ eclogite-facies metamorphic conditions estimated for the Zermatt–Saas zone in the Aosta Valley, Monte Avic Massif included (Dal Piaz et al., 2010, and references therein). In conclusion, the Monte Avic ultramafics record a long-lasting tectono-metamorphic history, implying the earliest (most likely ocean floor) pervasive serpentinization, followed by a typical orogenic evolution characterized by an initial high-$P$ metamorphism related to subduction and overprinted by a later greenschist-facies event connected to the exhumation.

The mineral assemblage indicates that the Monte Avic PS-15 veins formed at low $T$, most likely at the same time as the olivine alteration in the host metadunite, to give lizardite, brucite, and magnetite. This olivine breakdown, limited to the immediate vicinity of fractures, is due to the reaction with the hydrous fluids likely connected to the emplacement of the nearby PS-15 veins. On the contrary, within the vein, polygonal serpentine would be formed directly from the fluid. Similar constraints have been reported by Evans (2004) in a paper discussing the possible genetic conditions of "coexisting" chrysotile and lizardite. The author concludes that "Chrysotile growth is favored in isotropic stress microenvironments of fluid-filled voids and pores (where it may ultimately crystallize pervasively), and in veins, generally after active hydration in the immediate surroundings has ceased" allowing "the simultaneous growth of lizardite and chrysotile in adjacent partially and fully serpentinized peridotite, respectively". This explanation might also be valid for the Monte Avic veins, where the prevailing serpentine fibrous phase is PS-15 instead of chrysotile, but the same olivine alteration is observed in the nearby host rock.

Therefore, the genetic conditions of PS-15 are matching those of Ctl, since both minerals did grow in equilibrium in the same vein at the same time. However, while chrysotile typically grows as vein fillings of cross fibers and slip fibers, i.e., as sets of parallel fibers iso-oriented perpendicular ("cross" type) or parallel ("slip" type) to the vein selvages, PS-15 systematically grows as mass-fibers, i.e., as fibers oriented in all directions, as shown by the merging effects characterizing the homogenized μ-Raman data and confirmed by TEM images. These show that the veins consist of a felt of randomly oriented high-crystallinity PS-15 fibers with very minor chrysotile, surrounded by empty space, most likely originally filled by a hydrous silica-saturated fluid phase. The vein emplacement was accompanied by significant fluid pressure, as suggested by contact deformation and dismembering of the host rock during vein formation.

The random growth of the mass-fiber polygonal serpentine suggests that the mineral nucleated under hydrostatic pressure, with low-strain conditions and fluid supersaturation maintained by local potential gradients. The source of the infiltrating hydrous fluid is unknown, but certainly its origin cannot be related to the hydrothermal metamorphism connected to the opening of the Mesozoic Tethys ocean floor because PS-15 veins formed much later, towards the end of the long and polyphase Alpine tectono-metamorphic orogenic cycle, including an early subduction to eclogite-facies conditions, followed by a collisional phase characterized by exhumation under greenschist-facies peak conditions, followed by progressive cooling and decompression up to the Earth's surface. Although the problem of water origin in metamorphism has long been debated, unfortunately, at present it cannot be solved without a targeted chemical and isotopic study (Porowski et al., 2023).

In most rocks, the metamorphic evolution is accompanied by a repeated development of vein sets whose mineralogy reflects the prevailing regional P-T-X conditions. Based on the geometric crosscutting relationships among the different vein generations, it is possible to understand their relative emplacement chronology, as successfully done for the metamorphic ophiolites of both the Italian (see, e.g., Groppo and Compagnoni, 2007b) and Swiss sides (Kempf et al., 2020) of the Western Alps. In our case, the PS-15 veins have never been observed to cut other veins, thereby making this criterion impossible.

The mineralogy of the reaction rim between the PS-15 vein and the host metadunite (which is characterized by the stable coexistence of brucite, lizardite, and magnetite) indicates metamorphic temperatures lower than 300 °C (see, e.g., Evans, 2010), which may be assumed as a valid $T$ range for the Monte Avic PS-15 polygonal serpentine.

*Data availability.* No data sets were used in this article.

*Author contributions.* The manuscript and particularly the petrographic description were written by RCom and verified for accuracy by all authors. PC collected the samples and provided field data. Data acquisitions and their interpretations were carried out by GC for TEM, LP for XRPD, RCos for Raman spectrometry, and GF for hardness. LB prepared geologic maps and made photomicrographs. MM contributed to the general discussion.

*Competing interests.* The contact author has declared that none of the authors has any competing interests.

*Disclaimer.* Publisher's note: Copernicus Publications remains neutral with regard to jurisdictional claims in published maps and institutional affiliations.

*Acknowledgements.* The authors thank the BRIC 2019 project Caratterizzazione cristallochimica e studio della reattività di superficie di fibre minerali di interesse ambientale e sanitario ai fini di un'accurata analisi del rischio di contaminazione funded by INAIL with grant number 57.1 for supporting the dissemination of the results.

Micro-Raman spectra have been obtained with the equipment acquired by the Interdepartmental Centre "G. Scansetti" for Studies on Asbestos and Other Toxic Particulates with a grant from Compagnia di San Paolo, Torino, Italy. Comments by two anonymous referees greatly improved the manuscript. Thanks are also due to the editors Martine Buatier and Etienne Balan for their helpful assistance.

*Financial support.* This research has been supported by the Istituto Nazionale per l'Assicurazione Contro Gli Infortuni sul Lavoro (grant no. 57.1).

*Review statement.* This paper was edited by Martine Buatier and reviewed by two anonymous referees.

## References

Alberico, A., Belluso, E., Compagnoni, R., and Ferraris, G.: Amianti e minerali asbestiformi sul territorio piemontese, Giornata di studio su "Il rischio amianto legato alle attività estrattive ed alla bonifica di siti industriali dismessi", Torino, 20 maggio 1997, Associazione Georisorse e Territorio, e Regione Piemonte, Volume Atti, 97–102, 1997 (in Italian).

Baronnet, A. and Devouard, B.: Topology and crystal growth of natural chrysotile and polygonal serpentine, J. Cryst. Growth, 166, 952–960, 1996.

Baronnet, A. and Devouard, B.: Microstructures of common polygonal serpentines from axial HRTEM imaging, electron diffraction and lattice-simulation data, Can. Mineral., 43, 513–542, 2005.

Baronnet, A., Mellini, M., and Devouard, B.: Sectors in polygonal serpentine, a model based on dislocations, Phys. Chem. Mineral., 21, 330–343, 1994.

Belluso, E., Compagnoni, R., and Ferraris, G.: Occurrence of asbestiform minerals in the serpentinites of the Piemonte zone, western Alps, "Giornata di studio in ricordo del Prof. Stefano Zucchetti", Politecnico di Torino, 12 Maggio 1994, Vol. Contributi, 57–66, 1994.

Bigi, G., Castellarin, A., Coli, M., Dal Piaz, G. V., Sartori, R., Scandone, P., and Vai, G. B.: Structural model of Italy 1 : 500,000 sheet 1, CNR – Progetto Finalizzato Geodinamica, SELCA, Firenze, 1990.

Compagnoni, R. and Groppo, C.: Gli amianti in Val di Susa e le rocce che li contengono. Atti Convegno su "Amianto e Uranio in Val di Susa", Roma 2006, edited by: Sacchi, R., Covoni, D., and Micucci, L., Rend. Soc. Geol. It., 3, Nuova Serie, 21–28, 2006 (in Italian).

Compagnoni, R., Cossio, R., and Mellini, M.: Raman anisotropy in serpentine minerals, with a *caveat* on identification, J. Raman Spectrosc., 52, 1334–1345, https://doi.org/10.1002/jrs.6128, 2021.

Cressey, G., Cressey, B. A., Wicks, F. J., and Yada, K.: A disc with fivefold symmetry: the proposed fundamental seed structure for the formation of chrysotile asbestos fibres, polygonal serpentine fibres and polyhedral lizardite spheres, Mineral. Mag., 74, 29–37, 2010.

Dal Piaz, G. V., et al. (Eds.): Carta e Note illustrative del foglio 091 (Châtillon) della Carta Geologica d'Italia alla scala 1 : 50,000. APAT-Agenzia per la protezione dell'ambiente e per i servizi tecnici, Dip. Difesa del Suolo, Servizio Geologico d'Italia, 152 pp., 2010 (in Italian).

De Giusti, F., Dal Piaz, G. V., Massironi, M., and Schiavo, A.: Carta geotettonica della Valle d'Aosta, Mem. Scienze Geol., Padova, 55, 129–149, 2003 (in Italian).

Evans, B. W.: The serpentinite multisystem revisited: chrysotile is metastable, Int. Geol. Rev., 46, 479–506, https://doi.org/10.2747/0020-6814.46.6.479, 2004.

Evans, B. W.: Lizardite versus antigorite serpentinite: Magnetite, hydrogen, and life(?), Geology, 38, 879–882, https://doi.org/10.1130/G31158.1, 2010.

Evans, B. W. and Trommsdorff, V.: Regional metamorphism of ultramafic rocks in the Central Alps: Parageneses in the system CaO-MgO-$SiO_2$-$H_2O$, Schweiz. Miner. Petrog., 50, 481–492, 1970.

Groppo, C. and Compagnoni, R.: Ubiquitous fibrous antigorite veins from the Lanzo Ultramafic Massif, Western Alps, Per. Mineral., 76, 169–181, https://doi.org/10.2451/2007PM0014, 2007a.

Groppo, C. and Compagnoni, R.: Metamorphic veins from the serpentinites of the Piemonte Zone, western Alps, Italy: a review, Per. Mineral., 76, 127–153, https://doi.org/10.2451/2007PM0021, 2007b.

Groppo, C., Rinaudo, C., Cairo, S., Gastaldi, D., and Compagnoni, R.: Micro-Raman spectroscopy for a quick and reliable identification of serpentine minerals from ultramafics, Eur. J. Mineral., 18, 319–329, 2006.

Kempf, E. D., Hermann, J., Reusser, E., Baumgartner, L. P., and Lanari, P.: The role of the antigorite + brucite to olivine reaction in subducted serpentinites (Zermatt, Switzerland), Swiss J. Geosci., 113, 16, https://doi.org/10.1186/s00015-020-00368-0, 2020.

Krstanovic, I.: Serpentine mineral from Crni Kamen, Serbia, Neues Jb. Miner. Monat., 10, 451–465, 1997.

Logar, M.: Polygonal serpentine from Kačanik area, Annales Geologica Peninsula Balkanica, 56, 329–344, 1992.

Mellini, M.: Chrysotile and polygonal serpentine from the Balangero serpentinite, Mineral. Mag., 50, 301–305, 1986.

Mellini, M.: Structure and microstructure of serpentine minerals, in: Minerals at the Nanoscale, edited by: Nieto, F., Livi, K. J. T., and Oberti, R., European Mineralogical Union Notes in Mineral-

ogy 14, chap. 5, 1–27, https://doi.org/10.1180/EMU-notes.14.5, 2013.

Morandi, N. and Felice, G.: Serpentine minerals from veins in serpentinite rocks, Mineral. Mag., 43, 135–140, 1979.

Mugnaioli, E., Logar, M., Mellini, M., and Viti, C.: Complexity in 15- and 30-sectors polygonal serpentine: Longitudinal sections, intrasector stacking faults and XRPD satellites, Am. Mineral., 92, 603–616, 2007.

Petriglieri, J. R., Salvioli-Mariani, E., Mantovani, L., Tribaudino, M., Lottici, P. P., Laporte-Magoni, C., and Bersani, D.: Micro-Raman mapping of the polymorphs of serpentine, J. Raman. Spectrosc., 46, 953–958, 2015.

Porowski, A., Vinograd, N., and LaMoreaux, J.: Metamorphic Waters of the Earth's Crust: Origin, Occurrence and Applications, Springer Nature Switzerland AG, in preparation, 2023.

Rooney, J. S., Tarling, M. S., Smith, S. A. F., and Gordon, K. C.: Submicron Raman spectroscopy mapping of serpentinite fault rocks, J. Raman Spectrosc., 49, 279–286, https://doi.org/10.1002/jrs.5277, 2018.

Tarling, M. S., Rooney, J. S., Viti, C., Smith, S. A. F., and Gordon, K. C.: Distinguishing the Raman spectrum of polygonal serpentine, J. Raman Spectrosc., 49, 1978–1984, https://doi.org/10.1002/jrs.5475, 2018.

Tarling, M. S., Demurtas, M., Smith, S. A. F., Rooney, J. S., Negrini, M., Viti, C., Petriglieri, J. R., and Gordon, K. C.: Crystallographic orientation mapping of lizardite serpentinite by Raman spectroscopy, Eur. J. Mineral., 34, 285–300, https://doi.org/10.5194/ejm-34-285-2022, 2022.

Tartarotti, P., Benciolini, L., and Monopoli, B.: Brecce serpentinitiche nel massiccio ultrabasico del Monte Avic (Falda ofiolitica piemontese): possibili evidenze di erosione sottomarina, Atti Ticinensi Sci. Terra, Ser. Spec., 7, 73–86, 1998 (in Italian).

Varlakov, A. S.: A variety of serpentine with a lattice transitional between lizardite and clinochrysotile, as a rock-forming mineral in Alpine-type ultramafic rocks, Doklady Earth Science Sections, 278, 133–137, 1984.